J Indian Inst Sci, May–June 1998, **78**, 191–211

Applications of computation electromagnetics

N BALAKRISHNAN
Jawaharlal Nehru Centre for Advanced Scientific Research and Indian Institute of Science, Bangalore

Abstract

Electromagnetic systems form an integral and important part of all modern electronic system In their early stages of evolution, the design of electromagnetic systems stemmed on expensive will-and-try approach The advent of relatively inexpensive high-speed computers has made it possible to accurately predict the fundamental interaction of electromagnetic field with material bodies This led to the emergence of computational electromagnetics (CEM) as a field of great importance and scientific interest The central issue in CEM is the solutions of Maxwell's equations in a variety of physical media and geometrical environments

Over the last two decades, the Department of Aerospace Engineering at the Indian Institute of Science has actively pursued research in the broad area of aerospace electronic systems in general and CEM in particular The research is broad based and is of applied nature The complexity of the problems tackled by this group has grown over the years in tune with international developments in computing techniques and national needs In this paper, a sample of the research efforts in the broad area of CEM is presented

1. Introduction

The emergence of computational electromagnetics (CEM) can be attributed to two factors. Firstly, the electromagnetic systems in recent times have become an integral and important part of all modern electronic systems Further, the advent of relatively inexpensive high-speed computers has made it possible to accurately predict the fundamental interaction between electromagnetic fields and material bodies In their early stages of evolution, the design of electromagnetic systems stemmed on expensive build-and-try approach But, today, the level of maturity of CEM has ensured that experimental efforts are limited mostly to that of final validation The central issue in CEM is the solution of Maxwell's equations in a variety of physical media and geometrical environments

Over the last two decades, the Department of Aerospace Engineering at the Indian Institute of Science has been actively pursuing research in the broad area of aerospace electronics systems in general, and CEM in particular. The research work has been traditionally broad based and is of applied nature The complexity of the problems tackled by this group has grown over the years in tune with the international developments in computing techniques and the national needs In the early 80s, the major thrust of the group was towards designing antenna arrays with spatial and excitation constraints for applications including monopulse radars and also towards designing antennas mounted on a spacecraft [1-6] In this paper, a sample of the recent research efforts in the broad area of CEM is presented

2. Shape beam doubly curved reflector antennas for airborne applications

In airborne radars, the antenna is often mounted on top of the aircraft Due to practical considerations, such antennas have a larger aperture in the horizontal direction than in the vertical This leads to a radiation pattern that has a narrow beam in the azimuth plane and a broad beam in the elevation plane Conventional parabolic reflector antennas give Gaussian beams which, when broad, illuminate the ground with varying radiation intensities In order to illuminate the ground with constant power, the antenna is shaped appropriately so that the radiation pattern in the elevation plane has a cosecant-squared pattern Such antennas are called doubly curved reflector antennas The design problem in airborne radar antennas is that of designing the reflector shape so that it yields a prespecified cosecant-squared pattern in the elevation plane

One of the popular and simpler asymptotic techniques is the geometrical optics (GO) technique Using GO and the principle of conservation of energy, it is straightforward to determine the reflector shape for a given feed pattern However, the radiation characteristics of practical antennas are affected by diffraction from the antenna rim, scattering from struts that support the antenna and the blockage due to the feed Each of these has a geometrical shape and size that is unique to itself thus calling for combined application of several well-known CEM techniques

The central portion of the reflector in our work has been handled by aperture integration method In AI, the aperture plane in front of the antenna is discretised and the fields in each of the discretised cell are calculated by tracing the rays from the feed The far-field is then computed through aperture integration

The GTD is well developed for predicting the scattering from wedges This has been exploited to compute the diffraction from the antenna rim The struts are essentially cylindrical structures and are amenable to treatment as infinite cylinders The method of characteristic moments has been used to compute the effects of struts The feed blockage is treated using physical optics (PO) The above techniques are combined to accurately design and analyse doubly curved reflector antenna that yield prespecified shaped beam radiation

In order to verify the theoretical predictions, an S-band antenna of size 46 × 14 wavelengths has been used The feed has been chosen to yield a cosine squared function with –12 dB taper along the elevation plane The measured radiation pattern for the above antenna is available in literature Theoretical values as computed are plotted along with the experimental values in Fig 1 The closeness of the theoretical and the experimental results are seen clearly in Fig 1[7]

3. Instrument landing system

The instrument landing system (ILS) provides the pilot of an aircraft with steering information to make an accurate and controlled runaway approach and landing even under adverse weather conditions This is accomplished by the provision of azimuth guidance, elevation guidance and distance-from-threshold information

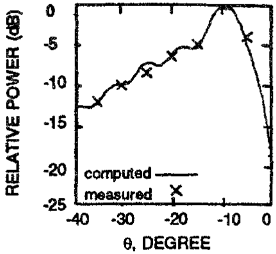

Fig 1 Shaped beam—experimental and theoretical

The main constituents of the ILS are the localiser, glide path and marker beacons The localiser, operating in the 108–112 MHz band, provides azimuth guidance information through the differential depth of modulation (ddm) of two signals at 90 and 150 Hz The ddm is zero on a vertical plane through the centre line of the runaway and varies linearly over the course sector The elevation guidance is provided by the glide-scope equipment in the 328–336 MHz band, also operating on the ddm principle with 50 and 150 Hz tones

Simultaneous nulling of the ddm from localiser and glide path equipment is expected to define a straight line descent path, at a desired elevation angle, lying in the vertical plane passing through the runaway centre line However, an aircraft on or near the glide path receives signals not only direct from the antenna system but also those reflected from the intervening terrain The effected terrain must be taken into account in determining the course provided by the glide path equipment

Most widely used antenna design makes use of reflection characteristics of an ideal ground to establish a proper glide path The design of arrays is based on image theory in which the ground plane is idealised as being infinite and perfectly conducting Since the elevation angles involved are small and wavelengths fairly large, wide stretches of plane ground must be available in front of the antenna to obtain a reasonable approximation to the ideal image patterns

The presence of unevenness, reflectivity fluctuations or other irregularities in the ground around the glide slope antenna causes kinks and bends in the electronically defined glide slope An aircraft trying to follow such a course is subjected to unnecessary maneuvers and, in extreme cases where the undulations come close to the ground or other obstructions, the result may be fatal Glide slope aberrations have been implicated in serious aircraft accidents in the past It is therefore clearly desirable to have an estimate of the quality of glide slope that may be obtained at specific ILS locations at the planning stage itself Such estimates can be obtained experimentally through actual inflight measurements with temporary installations However, such installations as well as flight calibration operations are very expensive More importantly, this procedure would only give glide slope data for the existing terrain and cannot provide insight into remedial measures such as terrain development, system reconfiguration, etc

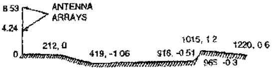

FIG 2 Six-segment idealisation of the terrain profile line at the airport (not to scale)

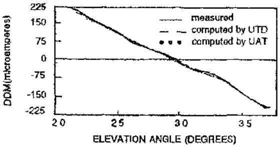

FIG 3 ddm at various elevation angles for a 1,000-foot level run at the airport profiled in Fig 2

Since the extent of terrain to be modelled is of the order of several wavelengths, asymptotic techniques are generally used Traditionally, PO and the physical theory of diffraction (PTD) have been applied in literature These techniques suffer either from lack of accuracy or from excessive computational effort required

In our approach, the uniform theory of diffraction (UTD) and uniform asymptotic theory (UAT) have been adopted to evaluate the terrain effects This was then applied with success to the measurement made at an airport in India

The terrain is first modelled using straight line segments resulting in a multi-wedge structure shown A computer algorithm has been developed to identify all the possible ray paths including the higher order rays such as reflected–reflected, reflected–diffracted, reflected–diffracted–reflected, etc [8]

Following the ray-tracing operation, the field contribution due to each ray that is found to exist may be computed using UTD or UAT Both the approaches have been applied to the ILS glide-path problem Real airport sites in India for which measured data are available have been chosen for validation. The starting point of the chain of computation is an aerial altimetry or a contour map of the site under evaluation The profile line derived from such a contour is then used to generate the plate model

Figure 2 shows the profile line for an existing airport approximated to a six-plate structure, up to a distance of 1,220 m from the glide-path antenna The ray tracing and field evaluation algorithms have been applied to this site, using both UTD and UAT, and the resulting fields are expressed in terms of equivalent ddm. These computed ddm values are compared with the measured values for validation of the theory

Two common experiments routinely conducted for ILS calibration are the level run and the low-level approach, standard procedures for which have been laid down by the ICAO Figure 3 is a plot of the ddm as a function of the elevation angle for a 1,000-ft-level run The measured values and the computed values are nearly coincident, and are very close to the measured curve over the entire run

The glide-path parameters derived from the level run are shown in the accompanying table along with measured values The difference between the measured and the computed path angles is only 0 02 degree The computed course width also agrees with measured values within an accuracy of 4%

The results for low-level approach run are shown in Fig 4 Here, both the computed ddm values along the nominal glide path remain throughout the run within the ICAO stipulation of 20 mirco amperes, as does the measured curve Subsequent efforts included the modeling of the terrain surface roughness and imperfect conductivity which improved the accuracy of prediction of the course bends in the glide-slope [9]

4. Characterisation of clutter echoes for airborne radars

Airborne radars are designed to detect targets against background echoes known as clutter Accurate knowledge of the clutter echoes is essential in the optimal design of the radar data processor This calls for the study of the scattering from different types of terrains, such as farm-land, urban-land, sea surface, etc , over which the radar may be required to operate Such characterisation of clutter echoes is accomplished by combining both analytical and experimental approaches World over, several countries have initiated successfully programs to characterise clutter echoes These have resulted in a substantial data base and empirical models However, they are often specific to the local geography and are not easily extendable to Indian conditions

In view of this, a clutter characterisation program was initiated to make measurements over Indian region and to develop theoretical models validated by the measurement The latter would make it possible to extend the analysis to arbitrary terrain and frequency

A non-coherent 'S' band radar with a pulse width of 800 ns and azimuth beam width of 1 6° was used for the measurements The radar was calibrated against standard trihedral corner reflector placed at different ranges The radar was calibrated first by mounting it on a hill top (at Nandi Hills near Bangalore, approximately 1 km above the fixed ground) Once calibrated, the radar was fitted in rotodome atop an aircraft and measurements were made over Kolar (a farm-land tract near Bangalore) and over the sea (Bay of Bengal). Two sorties were flown over Kolar on July 16, 1992 Sortie-I was flown at an altitude of 2 28 km above the ground and sortie-II at approximately 1 67 km above the ground On Sept 7, 1992, another sortie (sortie-III)

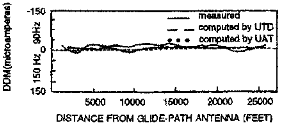

FIG 4 ddm along a nominal three-degree glide-path run at the airport profiled in Fig 1.

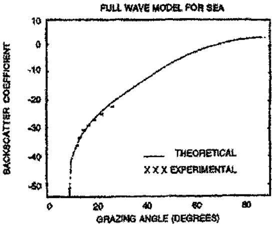

FIG 5 Variation of backscatter coefficient with grazing angle for the sea

was flown at an altitude of approximately 1 km. The measurements from this sortie yielded data from grazing angles as low as 2.8°. The sea clutter data was measured on July 17, 1992, using the airborne radar flown at an altitude of 2.28 km above the sea level. The wind speed was around 10–12 Kts and the sea state was 1 in the Beaufort scale during the measurements. During the airborne measurements, the aircraft was flown in an orbit of 4 km radius at 1°–s/ turn rate.

Mean σ_o measured at various grazing angles agreed well with those documented in literature. Statistical fluctuations in the σ_o was then modelled to characterise the clutter. The fluctuation has been quantified using log normal and Weibull distribution. The choice has been made because the Weibull probability density function has the advantage of having a mathematically tractable form and the log normal distribution function has been chosen to cater to long-tailed distribution of the measured data.

Two methods, viz. plotting on probability paper (PPP) and the maximum likelihood estimator (MLE) have been used to estimate the parameters of the distributions from the measured data for the farmland and the sea. It was found that a third-degree polynomial adequately fits the variations of the parameters of the Weibull and log normal distributions. The distribution parameters are also significantly different for farmland and sea implying that discrimination can be done using a well-trained neural network and with the distribution parameters as the feature vector. These observations and the model parameters are of critical value to the airborne radar designer.

Experimental approach to clutter characterisation has a limited utility, in that the measurements are specific to the radar used and the terrain over which the measurements are made. Duplicating the experiments over all terrains, frequencies and polarisation is an expensive proposition. To this end, a theoretical scattering model for the clutter echoes has been developed using full-wave analysis. Unlike the method of moments approach, full-wave analysis has the advantage that it can be applied to surfaces that are described in a statistical sense. Land and sea surfaces are described by dielectric constant, mean square height and correlation length. The theoretical approach can then be validated at spot frequency over which the measurements are available.

Figure 5 shows the experimentally measured and numerically obtained values of the mean σ_o for sea (Bay of Bengal). The experimental values of σ_o have been plotted from the data obtained during measurements conducted over Bay of Bengal on July 17, 1992. Theoretical and experimental models have been observed to agree well with each other in Fig. 5. Once the terrain parameters are established, at which the theoretical and measured σ_o values compare well, full-wave analysis can then be used to predict σ_o at other frequencies, polarisation and grazing angle.[10]

5. Scattering from weather targets

Weather radars transmit electromagnetic energy and measure the echo power. The reflectivity factor, Z, is a measure of the intensity of the echo and is proportional to the echo power. From Z, one could estimate the rain rate R, using a suitable R-Z relationship. Multi-parameter radars permit the estimation of more parameters besides Z For example, polarimetric radars measure the reflectivity factor at both horizontal (Z_H) and vertical (Z_V) polarisation and their ratio, the differential reflectivity, Z_{DR} Most polarimetric radars use coherent transmission and thus measure not only the mean Doppler and spectral width but also polarisation-related parameter such as specific differential phase shift K_{DP} and the correlation between horizontally and vertically polarised echoes, rho_{hv}

A long-standing problem in meteorology is that of distinguishing, by remote probing radars, between ice and water phases of precipitation This is especially challenging in convective storms, where water can exist at temperatures below 0°C and ice can be found at temperature above 0° C Virtually, all single and multi-parameter radar techniques conceived so far, have at one time or another been aimed at this problem Equally important is the problem of quantifying rain and hail fall rates when the precipitation is a mixture of the two

The contribution in this direction includes the development of a comprehensive framework for interpreting polarimetric radar data substantiated by CEM models for scattering from weather targets that addresses both the above problems

Using extensive scattering computations, parameters Z_H and K_{DP} that would be measured by a polarimetric radar when the precipitation is a mixture of hail and rain have been simulated. In these simulations, the size distributions of rain and hail have been obtained from earlier observations This is first plotted for various hail forms and rain and hail rates Superposing on this simulation results, the actual measurements of Z_H and K_{DP} from a storm before and after the hail fall gives an estimate of the rain and hail rates separately This demonstrated the utility of simulation in the identification of the presence of mixed phase precipitation and the quantification of rain and hail rates from the composite echo [11]

A significant contribution that was made includes the development of an algorithm that can be implemented in real time to estimate ρ_{hv} from time series data and the statistical and meteorological significance of ρ_{hv} [12] Rain and hail have different shape and size distributions as well as fall modes This manifests in the value of ρ_{hv} measured by the radar Extensive CEM simulations and comparison with actual radar measurements have shown that ρ_{hv} is an excellent tool for estimating the size of hail—a parameter of high utility in estimating crop damage and storm intensity [12]

Satellites are likely to be deployed in the future for global rain fall estimation For these measurements to be fruitful, the height of the rain column is to be predicted accurately. This can be done, once the melting layer is identified The correlation coefficient between horizontally and vertically polarised echoes has been measured with ground-based and airborne radars at nearly vertical incidence The data acquisition geometry and polarisation coordinates for the aircraft-based measurement are depicted in Fig 6

A sharp decrease in ρ_{hv} at the bottom of the melting layer has been observed This is in accordance with theoretical predictions of the scattering from an ensemble of randomly oriented prolate spheroids and/or distorted spheres The dominant factor that is seen to contribute to the ρ_{hv} decrease is seen to be the differential phase shift upon scattering[13] This has established the fact that a ground-based radar can be used to identify the height of the rain column and to cali-

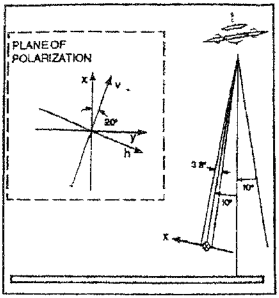

Fig. 6 Data-acquisition geometry and polarisation coordinates for aircraft-based measurements

brate the global rain rate measured by a satellite. The latter use is much in the same way a rain gauge is used to calibrate a radar.

The sophistication of the electromagnetic scattering models developed has been validated using a coordinated experiment. Polarimetric radar data consisting of complex weather signals at alternate vertical and horizontal polarizations were collected at 2109 h in a range-height mode. The National Oceanic and Atmospheric Administration (NOAA) P-3 aircraft, which was equipped with a two-dimensional cloud probe, executed a spiralling descent in the stratiform region starting at 2157 (7 km above the ground level (agl)) and ending at 2229 (2.7 km agl). A radiosonde was launched through the system from the National Severe Storms Laboratory (NSSL) mobile-class (M-class) platform at 2243. This sounding provides profiles of pressure, temperature, water vapour, and horizontal wind from the stratiform region. (The loran signal was lost for a portion of the flight, hence no middle-level winds were obtained.) Data from the M-class and aircraft descent sounding were used to determine the temperature profile for interpretation of radar measurements. From those soundings, the melting level was determined to be at 3.4 km. The weather signals were processed to produce the reflectivity factor Z, the differential reflectivity Z_{DR}, the correlation coefficient between copolar echoes $|\rho_{hv}|$, and the two-way differential propagation constant K_{DP}.[11,12]

A sample output of height profile of average reflectivity from the ground radar, the radar of the P-3 aircraft and the electromagnetic scattering model is given in Fig. 7. The close agreement among the three measurements is a testimony to the fact that the EM scattering computations when properly used with radar measurements provide a framework for distinguishing by remote probing various types of precipitation. This has culminated in a more sophisticated mapping of a vertical profile of a storm (Fig. 8).[14] This provides invaluable input into the understanding of microphysics.

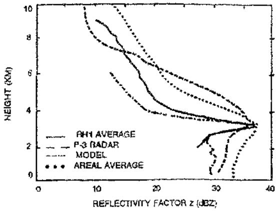

FIG 7 Height profiles of average reflectivity comparisons

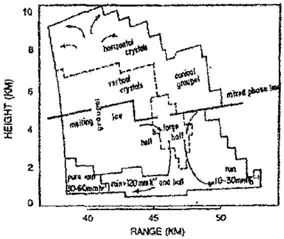

FIG 8 Sche[illegible] the range height [illegible]

Since the weather targets are of sizes of the order of the wavelength, conventional MoM techniques may not be adequate Hence, electromagnetic scattering calculations that formed the basis in the identification and classification of the weather targets have been done using T-matrix method T-matrix method is well suited for handling large scatters of complex geometry and material characteristics The only restriction that the T-matrix method poses is that the geometrical shape of the scatterer must be smooth with continuous first derivative. Further, polarisation is inherent in the formulation T-matrix is also ideally suited for handling multilayered (coated) scatterers

6. Radar cross-section control and management using chiral polymers

Although the radar cross-section (RCS) of a body is determined significantly by its shape, what the medium is composed of also plays an important role[15] From RCS point of view, the most important property of composite materials is that they reflect electromagnetic waves less than metals The exact constituent and primary constants (μ_r, ε_r and σ) of the composite materials that are used for RCS reduction are either classified or trade secrets, essentially, they are graphic fabric epoxy resins or thermo plastics matrix-graphic composites To achieve zero reflectivity for electromagnetic waves, the constituent parameters of the material must satisfy certain conditions not ordinarily satisfied by conventional radar-absorbing materials (RAMs)

Chiral composites[16,17] provide an additional degree of control that makes them better suited for use in the reduction of RCS. Chirality refers to the lack of geometric symmetry between an object and its mirror image. The mirror image of a chiral object cannot be made to coincide with the object involving rotations and/or translations Some common chiral objects are helices, Mobius strips and gloves Materials that are made up of such micro structures with handedness exhibit different propagation characteristics for left and right circularly polarised waves Some natural materials possess chirality at optical frequencies and hence chirality is also known as *optical activity*.

With recent advances in polymer science, it has now become possible to manufacture materials which possess chirality at low frequencies.[18] Planar chiral samples can be made by embedding large number of micro miniature helices in a host material. The property of such materials can be controlled by altering the size and concentration of the embedded particles, to yield prespecified chirality.

The introduction of chirality complicates Maxwell's equations in that the propagation constants are different for left and right circularly polarised waves. Further, since the chiral materials are merely used as coatings, the need arises to develop techniques that will be able to theoretically predict the scattering from layered materials. The extended boundary condition method (EBCM) or the transition matrix (T-matrix) method[19] has several properties that make it ideally suited for this purpose. As evidenced by our earlier work on weather targets, T-matrix method is well suited for handling large-sized arbitrarily shaped, layered scatterers and has been successfully applied to the prediction of RCS of chirally coated bodies.[20]

In order to evaluate the effectiveness of the chiral coatings on canonical and arbitrary-shaped objects in reducing RCS, two kinds of chiral materials have been used. They are the RAM-type chiral polymers and realistic chiral polymers.

- *RAM-type chiral polymers* were used such that permittivity and permeability were assumed to be the same as that of the RAM and the chirality parameter β was added. The properties of RAM-type chiral polymers were chosen such that the relative permittivity and the chirality parameter were assumed to be independent of frequency. The relative permeability was assumed to be unity.

The results are presented for a chiral and RAM-coated conducting sphere. It is first coated with a RAM of dielectric constant $1.3 + i0.29$ at 10 GHz. The coating thickness was taken to be 0.4 cm. The variation of scattering parameters with $k_o a$ is shown in Fig. 9. Also included in the figure is the RCS of a conducting sphere. It is seen that there is a reduction of 2–3 dB by RAM coating.

Next, chirality is added to RAM and the results are shown for two values of $\beta = 0.2$ and 0.3 cm. The normalised RCS is reduced by 2 dB for the RAM coating and by about 5 dB for a chiral coating of $\beta = 0.2$ cm. The reduction in RCS has been found to be about 15 dB for the chirally coated perfect conductor for $\beta = 0.3$ cm. The Mie oscillations are absent when the sphere is coated with a chiral material. There is an increase in the absorption cross-section from 0.5 for a RAM coating to 1.2 for a chiral-coating sphere. The scattering cross-section reduces from 3 dB for a RAM to 0 dB for chiral coating.

To study the effect of chiral coatings on arbitrary-shaped bodies an oblate conducting spheroid is taken as a typical example. Generalised EBCM has been used to analyse such bodies. Results for the variation of the scattering characteristics as a function of size parameter were computed using the code developed.

To illustrate the effect of diameter variation as a function of the normalised scattering parameters, a RAM of $\varepsilon_2 = 1.3 + i0.29$ at 10 GHz has been chosen as earlier. The inner layer has been taken as a conductor of equivalent radius r_1. This is the base against which the extent of RCS modification by RAM and chiral coating are compared. The coating thickness is fixed at 0.4 cm. The axis ratio for the inner layer a_1/b_1 has been chosen to be 0.8. The outer aspect ratio

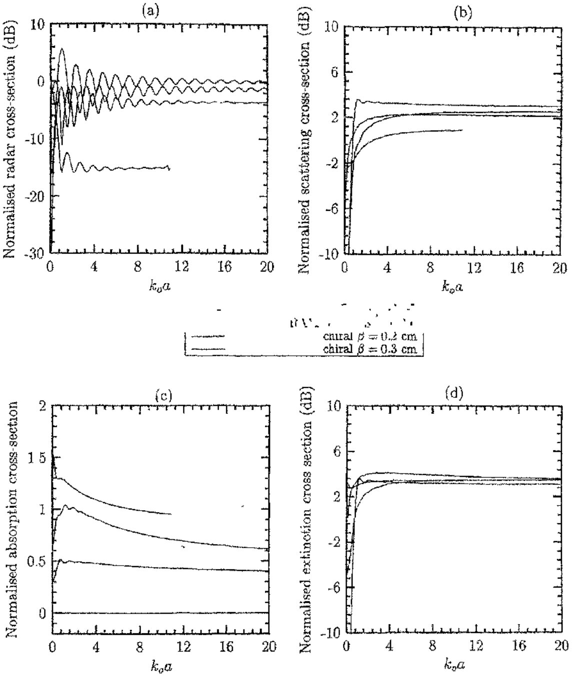

FIG 9 Variation of scattering characteristics with $k_o a$ (a) Normalised radar cross-section, (b) Normalised scattering cross-section, (c) Normalised absorption cross-section, (d) Normalised extinction cross-section

will be slightly different due to coating thickness The plots as shown in Fig 10 are for a conducting oblate spheroid, coated by a RAM, and by a RAM-type chiral polymer, for horizontal polarisation Chirality has been introduced in the RAM material so as to represent achiral RAM-type polymer To this end, the intrinsic ε_2 has been taken as that of the RAM The values of β that have been considered are 0.2 and 0 3 cm These values ensure that the propagation constants for the LCP and the RCP waves (k_L and k_R) are positive numbers As can be observed

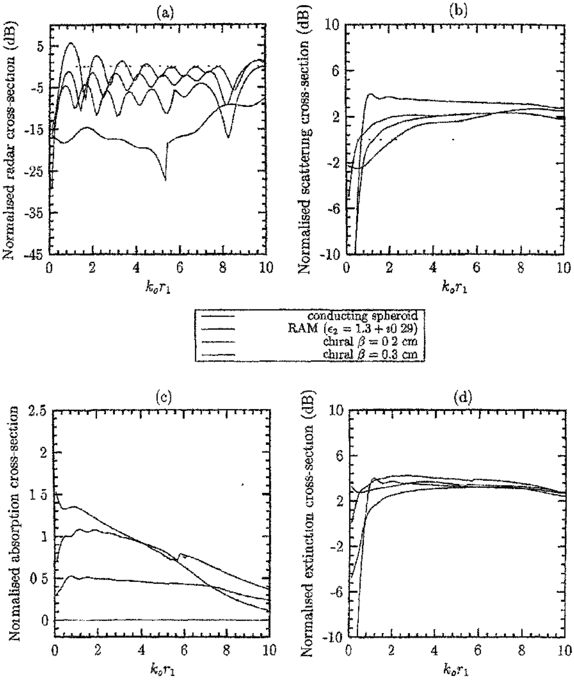

FIG 10 Variation of scattering characteristics with $k_o r_1$ (a) Normalised radar cross-section, (b) Normalised scattering cross-section, (c) Normalised absorption cross-section, (d) Normalised extinction cross-section, for a chirally coated oblate spheroid of axis ratio = 0 8, $\lambda = 3$ cm, coating thickness = 0 4 cm for horizontal polarisation

from Fig 1, the Mie oscillations have smoothened, which is an indication of increased bandwidth

In the case of horizontal polarisation of the incident field, the normalised RCS for chirally coated spheroid has been found to be below 15 dB for $k_o r_1$ varying up to a value of 7, whereas the reduction in RCS is only 2–3 dB for a RAM-coated body (Fig 10(a)) The normalised absorption cross-section for a chirally coated spheroid has value 1 on an average for $k_o r_1$ varying from 0 to 4 5 This value is higher than that for the RAM-coated spheroid Scattering and extinction cross-sections have been found to be only slightly different for RAM and chirally coated bodies, the scattering cross-section being lesser for chiral than for a RAM coating

- *Realistic chiral polymers* In the RAM-type chiral polymers, the constitutive parameters were assumed to be independent of the frequency and the relative permittivity was chosen to be unity Such a treatment is not appropriate while dealing with chiral media These chiral materials are made by embedding miniaturised helices in a low-loss host medium Thus, even though chiral inclusions are non-magnetic to begin with, the composite medium will have magnetic properties The effect of scattering characteristics of objects (both canonical and arbitrary shaped) coated with such realistic chiral materials is presented in this paper

To compare the scattering characteristics of a conduction sphere coated with a RAM and a realistic chiral polymer, a RAM of $\varepsilon_2 = 1\ 3 + i0\ 29$ has been chosen at a frequency range of 8–13 GHz Permeability has been assumed to be unity, and independent of frequency RCS of the RAM-coated conducting sphere has also been included in Fig 11(a and b) for coating thickness $t = 0\ 1$ cm and $t = 0\ 5$ cm, respectively RCS for a 0 1 cm coating thickness using RAM and 1 6% concentration of right-handed helices is similar as seen from Fig 11(a) However, the finite size of the helices needed for measurable chirality at microwave frequencies demands that the coating thickness be larger than $t = 0\ 5$ cm Hence, computations have been made at $t = 0\ 5$ cm RCS for 1 6% concentration and $t = 5$ cm coating thickness is plotted in Fig 11(b) for a frequency range of 9 76–11 63 GHz It is clear that for $t = 0\ 5$ cm coating with 1 6% concentration of right-handed helices reduces the RCS by 7 dB from 3 5 dB (for $t = 0.1$ cm) for $t = 0\ 5$ cm RAM coating

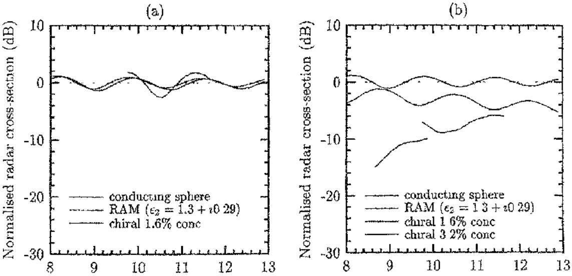

FIG 11 Variation of the normalised radar cross-section with frequency for (a) $t = 0\ 1$ cm and (b) $t = 0\ 5$ cm

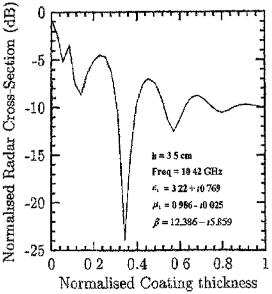

FIG 12 Variation of the normalised radar cross-section of a chiral-coated conducting sphere, with normalised coating thickness

In order to appreciate the effect of concentration, computations of RCS have been carried out for the 3 2% concentration and 0 5 cm-coating thickness in the frequency range 8 66–9 87 Hz This, as seen from Fig 11(b), has reduced RCS to less than 10 dB

In most cases of scattering from coated surfaces, RCS variations would exhibit Mie oscillations as the coating thickness is varied This is depicted in Fig 12 wherein RCS is plotted as a function of coating thickness The frequency is chosen to be 10 42 GHz, and a 1 6% concentration chiral composite is used RCS for thicknesses larger than 1 cm reduces by 10 dB [21] The variations at other frequencies are similar and hence are not included

For studying the effect of realistic chiral coating on an arbitrary-shaped object a conducting oblate spheroid is chosen For the purpose of comparison, a practical RAM was chosen from Bhattacharya and Sengupta[15] of $\varepsilon_r = 1.3 + i0\ 29$ An oblate conducting spheroid was coated by such a RAM and the coating thickness was kept fixed at $t = 0\ 5$ cm as that of chiral coating Outer aspect ratios were chosen to be 0 8 The outer equivolume diameter was kept at 6 cm, the same as that for chiral coating RCS of the conducting oblate spheroid coated by a conventional RAM is compared with the chirally coated spheroid The response is shown for the frequency range of 8–12 GHz RCS comparison between the two coatings has been shown for both horizontal and vertical polarisations (Fig 13) It can be seen from the plots that, for the same coating thickness, RCS for a RAM coating gets reduced by 5 dB, as compared to a reduction of more than 15–20 dB when coated by a realistic chiral material This was seen in both horizontal and vertical polarisations.

The variation in the normalised RCS and absorption cross-section as a function of the angle of incidence for RAM and chiral coating is shown in Fig 14 The frequency has been fixed at 9 87 GHz The values for complex permittivity, complex permeability and complex

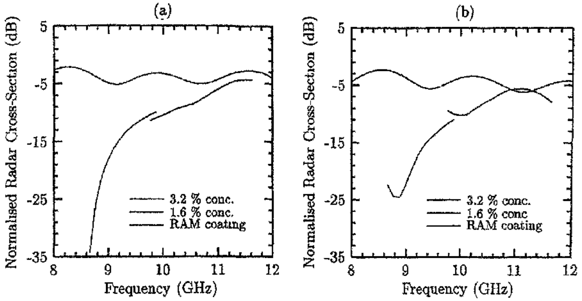

Fig 13 Variation of the normalised radar cross-section with frequency, for a RAM and a chiral-coated oblate spheroid of an aspect ratio of 0.8, for (a) horizontal, and (b) vertical polarisation

chirality are $\varepsilon_r = 3.529 + i3.731$, $\mu_r = 0.820 - i0.353$ and $\beta = (18.091 - i12.01) \times 10^{-3}$ cm These are for RCP helices embedded in the host medium with a 3.2% volume concentration The results are compared with a conventional RAM coating of $\varepsilon_r = 1.3 + i0.29$ at 9.87 GHz The coating thickness is kept the same as that for the chiral coating. An aspect ratio of 0.8 has been chosen for the RAM As seen from the graphs, normalised RCS for RAM-coated oblate spheroid for this particular frequency is less than that for the chirally coated spheroid The reduction in RCS is over a larger aspect angle clearly indicating a wider bandwidth The absorp-

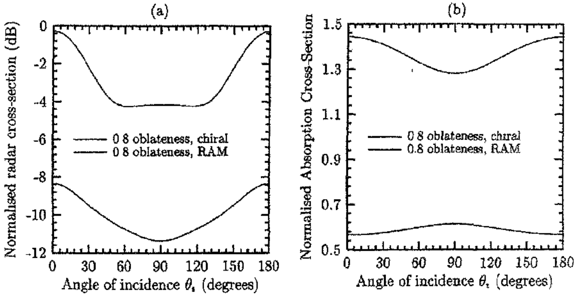

Fig. 14 Variation of (a) normalised radar cross-section, and (b) normalised absorption cross-section for a RAM and a chiral-coated oblate spheroid for an aspect ratio of 0.8, with angle on incidence

tion cross-section for the RAM-coated conducting spheroid has been found to be 0 55 as compared to 1 4 for a chirally coated case

7. Target recognition

Conventional radars are merely devices for detecting the presence of a target and to estimate their range They use simple continuous wave (CW) or burst EM for transmission and reception In recent times, there have been considerable improvements in the technology of generating high-power short-duration wideband signals. The availability of high-speed computers has in fact enabled the development of high-resolution methods of simulation These factors contributed to the birth of applications of radars for target recognition and classification.

Radar-target recognition methods are analogous to those employed in system identification wherein either the impulse or the frequency response is used for identifying the system The methods that are used in radar-target recognition are depicted in Fig 15 The two methods, viz E-pulse and finite-difference time domain (FDTD), are described below

Radar targets such as the aircraft are several wavelengths long Short-duration pulses take a finite time to propagate across the target The echo from the target, if analysed in time domain with higher resolution, will reflect the target characteristics Experience from circuit theory has shown that such characteristics can be identified from the location of the poles This will lead to the features of the target that are independent of the aspect and incident polarisation

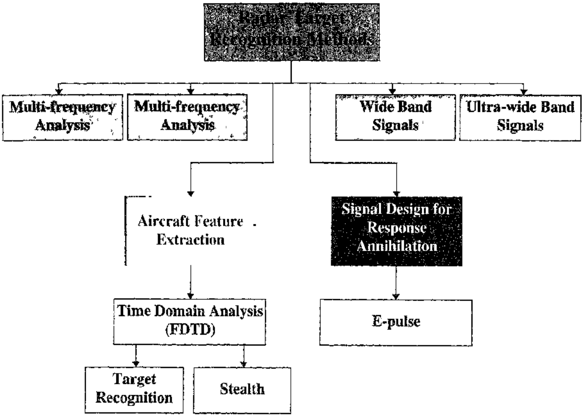

FIG 15 Radar target-recognition methods

The singularity expansion method (SEM) is combined with the method of moments (MoM) to obtain the natural response of the target Then, this is used to obtain the E-pulse which is an excitation waveform synthesised so as to minimise the transient scattered field response In other words, E-pulse is a transient, finite-duration waveform which annihilates the contribution of a select number of resonances in late time response Target discrimination results from a unique correspondence of an E-pulse to a particular target Excitation of dissimilar targets yields higher response Thus, one could have a library of E-pulses for the targets that need to be discriminated and convolve the echo from the actual target with that stored in the library and thus classify the targets

The second approach that leads to better understanding of the echo from the target is based on FDTD method In the FDTD, a differential equation is replaced by its corresponding difference equation, which is obtained by replacing various orders of derivatives by their finite-difference approximations The finite-difference approximation to any derivatives of a function is obtained from the Taylor's series expansion of the function Different kinds of difference approximations that may be used are the forward, backward and central difference

Forward and backward differences can be used to approximate the first-order derivatives However, central difference can be used to approximate both the first- and the second-order derivatives since it gives the least error

In electromagnetics, Maxwell's curl equations were first approximated using central difference approximations, by Yee[22] in 1966 He interleaved the electric and magnetic field components in space and time, in a cuboid of dimension $\Delta x \times \Delta y \times \Delta z$, called the Yee unit cell shown in Fig 16, so as to permit a natural satisfaction of the continuity of the tangential field components at media interfaces The electric field is updated at every Δt and the magnetic field at every $\Delta t + 0\ 5$ time step

The FDTD method is very simple in concept and execution, yet is remarkably robust, providing highly accurate modelling predictions for a wide variety of electromagnetic wave interaction problems It does not employ any potentials, but is a simple second-order accurate central-difference approximation for space and time derivatives of the electric and magnetic fields FDTD works well both for conducting and dielectric materials, which may be homo- or inhomogeneous, iso-, aniso- or bianisotropic, single- or multilayered Differential equations being local in nature can be used to analyse objects which have sharp corners (complex objects) and also for narrow pulses The required computer storage and running time is dimensionally low, proportional only to N, where N is the number of electromagnetic field unknown in the volume modelled [23]

The greatest disadvantage of the FDTD is that the entire computational domain has to be discretised, thus requiring a lot of computer storage However, this difficulty has been overcome by restricting the computational domain to a smaller area by introducing absorbing boundaries Many methods find mention in literature, some of them are Yee's[22] and Mei's boundary conditions[24] and the perfectly matched layer (PML)[25] computational run

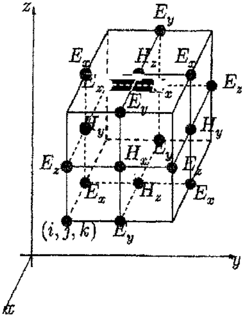

FIG. 16 Yee unit cell

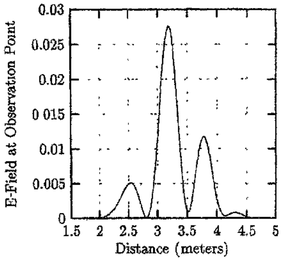

FIG. 17 RCS of an aircraft

Out of the above-mentioned boundary conditions, the PML boundary condition is the most popular. PML absorbs the electric and magnetic field components by splitting the electric and magnetic fields into two subcomponents each. These subcomponents are absorbed by using different electric and magnetic conductivities in different directions. However, the ratio of the magnetic-to-electric conductivity, in a given direction, is kept equal to the square of the intrinsic impedance of free space. As the time rate of absorption is high in the PML one has to make use of the exponential time-stepping scheme.

PML has an absorption of about 70 dB down over a wide band of frequencies and at all angles of incidence. It also has a global error power of about 10^{-11} over the entire computational run.

Figure 17 shows the radar cross-section of an aircraft when incident by a pulse having a pulse width of 3.3355 ns (or 1.0 m). As can be seen from the figure, there are three peaks which are reflections from the nose, the wings and the tail of the aircraft, respectively. In Fig. 18, the currents on the aircraft are shown at four different time steps. The spots which contribute to larger reflections and hence to the enhancement of RCS are clearly identified in Fig. 18. The absorbing paints can be applied only at these spots and this would lead to enormous saving in cost and reduce the weight penalty for the aircraft.

8. Conclusions

The power of the techniques in computation electromagnetics in solving a wide variety of problems including antenna design, spacecraft-mounted antenna, scattering from land and sea surfaces, site diversity for ILS, identification, classification and estimation of precipita-

(a) Time 7 3381 ns (b) Time 10 6736 ns

(c) Time 16 6775 ns (d) Time 20 6801 ns

FIG 18 Currents on the surface of the aircraft for a pulse incident on the nose, with a pulse width of 2 6684 ns, moving towards the tail

tion habitats, RCS reduction of aircraft and target *identification has been demonstrated* The major strength of the work is that in all cases, appropriate experimental verification that formed part of the national and international initiatives have been carried out This has in a large measure increased one's confidence in the sophistication of the CEM techniques described in this paper

References

1 Balakrishnan, N , Murthy, P K and Ramakrishna, S — Synthesis of antenna arrays with spatial and excitation constraints, *IEEE Trans* , 1979, **AP-27**, 690–696

2 Balakrishnan, N and Ramakrishna, S — Optimum difference mode excitations for monopulse arrays, *IEEE Trans* , 1982, **AP–30**, 325–330

3 Bokhari, S A and Balakrishnan, N — A wire grid model for the analysis of VHF antennas mounted on the Bhaskara satellite, *Proc Int Symp Antennas and Propagation (ISAP),* Kyoto, Japan, 1985, pp 1139–1141

4 Bokhari, S A and Balakrishnan, N — Analysis of cylindrical antennas—a spectral iteration technique, *IEEE Trans* , 1985, **AP–33**, 251–258

5 Bokhari, S A and Balakrishnan, N — A spectral iteration technique for analysis of Yagi-Uda arrays, *Proc IEE* (Lond), Part-H, 1985, **3**, 198–202

6 Bokhari, S A and Balakrishnan, N — A method to extend the spectral iteration technique, *IEEE Trans* , 1986, **AP–34**, 51–57

7 Shridhar, B S and Balakrishnan, N — Accurate design of shaped beam doubly curved reflector antennas for airborne applications, *Proc Twelfth Ann Rev Progr in Computational Electromagnetics*, Naval Postgraduate School, Monterey, California, USA, 1996

8 Poulose, M M , Mahapatra, P R and Balakrishnan, N — Computer aided ILS site evaluation deemed practical, *Commonw Air Transp Electronics News*, 1987, **26**, 9–12

9 Poulose, M M , Mahapatra, P R and Balakrishnan, N — Terrain modelling of glide slope for ILS, *Proc IEE* (Lond), 1997, **134**, 275–279

10 Menon, K R , Balakrishnan, N , Shenoy, R P and Ramchand, K — Characterisation of land and sea clutter from air-borne measurements, *Proc Int Conf on Radar*, Paris, 1994, pp 173–178

11 Balakrishnan, N and Zrnic, D S — Estimation of rain and hail rates in mixed phase precipitation, *J Atmos Sci* , 1990, **47**, 565–583

12 Balakrishnan, N and Zrnic, D S — Use of polarisation to characterise precipitation and discriminate large hail, *J Atmos Sci* , 1990, **47**, 1525–1540

13 Zrnic, D S , Balakrishnan, N , Ryshkov, A and Durden, S L — Use of copolar correlation coefficient for probing precipitation at nearly vertical incidence, *IEEE Trans* , 1994, **GRS-32**, 740–748

14 Zrnic, D S , Bringi, V N , Balakrishnan, N , Aydin, K , Chandrashekar, V and Hubbert, J — Polarimetric measurements in a severe hailstorm, *Mon Weath Rev* , 1993, **121**, 2225–2238

15 Bhattacharya, A K and Sengupta, D L — *Radar cross section analysis and control*, Artech House, 1991

16 Lakhtakia, A , Varadan, V K and Varadan, V V — *Time harmonic electromagnetic fields in chiral media*, Springer–Verlag, 1985

17 Lindell, I V , Sihvola, A H , Tretyakov, S A and Viitanen, A J — *Electromagnetic waves in chiral and bi-isotropic media*, Artech House, 1994

18 Ro, R — *Determination of the electromagnetic properties of chiral composites using normal incidence measurements*, Ph D thesis, The

Pennsylvania State University, University Park, Pennsylavania, 1991

19 Lakhatia, A, Varadan, V K and Varadan, V V — Scattering and absorption characteristics of lossy, dielectric, chiral, non-spherical objects, *Appl Opt*, 1985, **24**, 4146–4154

20 Sharma, R, Balakrishnan, N, Varadan, V V and Varadan, V K — Scattering from chirally coated spherical conductor, *J Wave Material Interaction*, 1994, **9**, 17–34

21 Sharma, R and Balakrishnan, N — Scattering from chirally coated bodies, *Appl Electromagnetics Society, Symposium*, Monterey, California, USA, 1996

22 Yee, K S — Numerical solution of initial boundary value problems involving Maxwell's equation in isotropic media, *IEEE Trans*, 1996, **AP-14**, 302–307

23 Taflove, A and Umashankar, K R — Review of FD-TD numerical modelling of electromagnetic wave scattering and radar cross section, *Proc IEEE*, 1989, **77**, 682–699

24 Mei, K K, Pous, R, Chen, Z, Liu, Y-W and Prouty, M D — Measured equation of invariance A new concept in field computations, *IEEE Trans*, 1994, **AP-42**, 320–328

25 Berenger, J-P — A perfectly matched layer for the absorption of electromagnetic waves, *J Computational Phys*, 1994, **114**, 185–200